# Highly Enhanced Concentration and Stability of Reactive $Ce^{3+}$ on Doped $CeO_2$ Surface Revealed *In operando*

*William C. Chueh[1,2,*], Anthony H. McDaniel[1], Michael E. Grass[3], Yong Hao[2], Naila Jabeen[3,4], Zhi Liu[3], Sossina M. Haile[2], Kevin F. McCarty[1], Hendrik Bluhm[5], Farid El Gabaly[1]*

[1]Sandia National Laboratories, Livermore, California 94551, United States

[2]Materials Science, California Institute of Technology, Pasadena, California 91125, United States

[3]Advanced Light Source, Lawrence Berkley National Laboratory, Berkeley, California 94720 United States

[4]Nanosciences & Catalysis Division, National Centre for Physics, Islamabad 44000 Pakistan

[5]Chemical Sciences Division, Lawrence Berkley National Laboratory, Berkeley, California 94720 United States

## Supplementary Information

### *Photolithography Procedure*

Metal patterns were fabricated by metal liftoff photolithography. Positive photoresist (Shipley 1813) was spin-coated onto YSZ substrates at 2,000 to 3,000 rpm and baked at 115 °C for 150 s. The sample was then aligned with the glass plate mask using a Karl Suss MJB 3 contact aligner and exposed to UV

light for 45 to 75 s. Next, the photoresist was developed by immersing the sample in Microposit MF-319 solution for ~ 30 to 60 s. After rinsing by deionized water and drying, the sample was cleaned using an oxygen plasma to remove residual organics and then transferred to a DC magnetron sputtering system (AJA International) where Pt (99.99 % purity) was deposited in 3 milltorr Ar. The growth rate was approximately 10 nm $min^{-1}$ and the total thickness approximately 200 nm. Metal liftoff was performed by immersing the samples in acetone at room temperature. The above procedure was repeated for the other side of the substrate to make a symmetric cell.

***Additional Physical Characterization***

Epitaxy of the film was confirmed by X-ray diffraction (Figure S1). In-plane diffraction pattern shows the expected four-fold rotation symmetry of the (220) peak when the (200) oriented sample was titled by 45 ° and rotated about the sample normal axis. Furthermore, the SDC thin film shows excellent registry alignment with the YSZ substrate. Out-of-plane diffraction pattern only contained the (200) family peaks, again confirming the eptixay. The rocking curve yielded a full-width half-max of 0.30°. A cross-sectional scanning electron micrograph of a typical sample, Figure S2, shows the two morphological regions of SDC: columnar-type growth over Pt and epitaxial growth over YSZ.

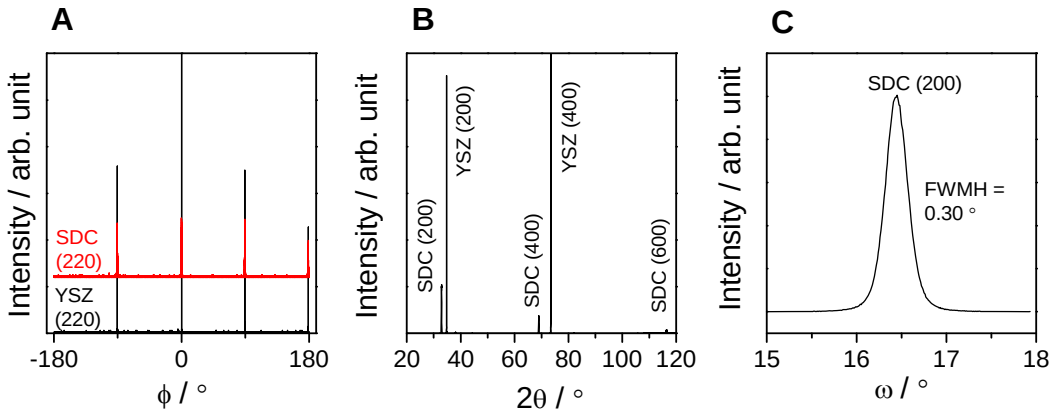


**Figure S1.** (a) In-plane, (b) out-of-plane, and (c) rocking curve X-ray diffraction pattern for SDC(100) without the burried Pt electrical contacts. Cu kα X-ray source (45 kV, 40 mA) was used.

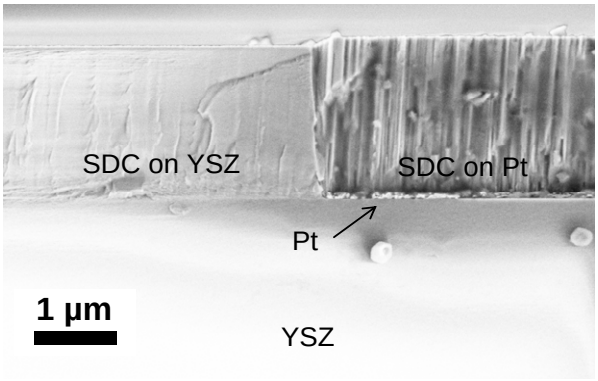


**Figure S2.** Cross-sectional scanning electron micrograph of SDC(100) with buried electrical contacts.

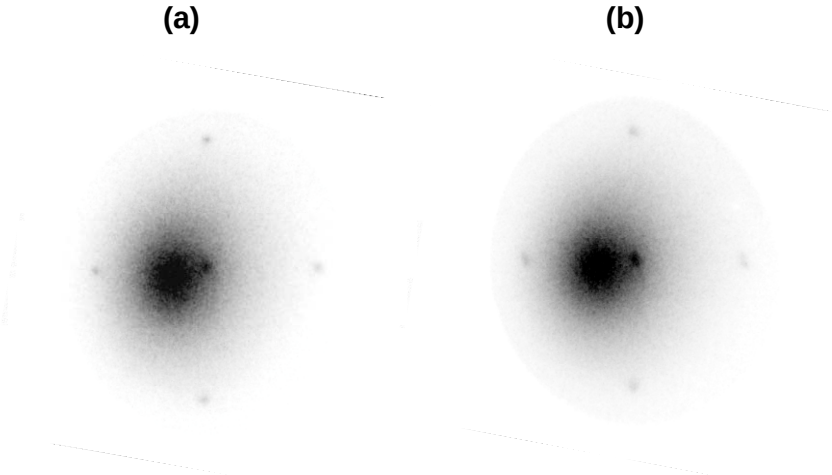


**Figure S3.** *In-situ* low-energy electron diffraction patterns for SDC collected at **(a)** $1.8 \times 10^{-6}$ Torr $O_2$ , 740 °C (oxidizing condition) and **(b)** $1.0 \times 10^{-7}$ Torr $H_2$, 600 °C (reducing condition) using 19 eV electrons. The patterns are consistent with a first-order diffraction from SDC(100). These diffuse features are due to secondary electrons.

***Electrochemical Impedance Spectroscopy***

A one-dimensional Poisson-Nernst-Planck transport model has been proposed and validated for the thin film solid-state electrochemical cell utilized here.[1,2] This transport model, discussed briefly below, is used to determine the bulk oxidation state, $[Ce^{3+}]_{bulk}$ , from the impedance response. We consider mixed oxygen vacancy and electron conducting thin films grown on both sides of a pure ion-conducting

substrate. Because of the aspect ratio of the thin films used here, the rate of oxygen incorporation and release upon perturbation in SDC is limited by surface reactions rather than by bulk transport. By further supposing that oxygen ion transfer across the ceria-gas external interface is the rate-limiting step, the model predicts a single half-circle arc in the Nyquist plot described by the following equivalent circuit:

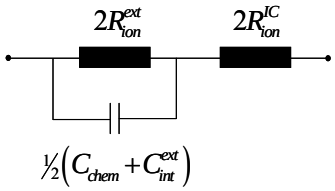


where $R_{ion}^{IC}$ is the resistance of the YSZ ion-conducting substrate, $C_{chem}$ is the chemical capacitance, and $C_{ion}^{ext}$ and $R_{ion}^{ext}$ are the surface capacitance and reaction resistance (for the external ceria-gas interface), respectively. The factors of 2 and ½ account for the fact that the electrochemical cell is symmetric. The chemical capacitance, in particular, is the variation in oxygen stoichiometry upon a variation in the chemical potential:

$$C_{chem} = e^2 V \left( \frac{1}{z_{ion}^2} \frac{d\mu_{ion}}{dc_{ion}} + \frac{1}{z_{ion}^2} \frac{d\mu_{eon}}{dc_{eon}} \right)^{-1} \quad \textbf{(S1)}$$

where $V$ is the thin film volume, $e$ is the electron charge, $z$ is the formal charge, $\mu$ is the chemical potential, and $c$ is the defect concentration. Subscripts "ion" and "eon" denote the ionic defect (oxygen vacancy in this case) and the electronic defect (polarons), respectively. In heavily-doped ceria such as the SDC, the bulk defect chemistry is well-known.[3] Under the dilute-solution limit, the chemical potential for both defects can be expressed as $\mu_i \approx \mu_i^0 + k_B T \ln c_i / c_i^0$. Finally, we recognize that under moderately reducing conditions, the oxygen vacancy concentration is fixed by the dopant concentration ($c_{ion} \approx \frac{1}{2} c_{dop}$). Combining these expressions with Eq. (S1), we obtain the following relationship between the chemical capacitance and the electron concentration:

$$c_{eon} = \left( \frac{e^2 V}{C_{chem} k_B T} - \frac{1}{2c_{dop}} \right)^{-1} \quad \textbf{(S2)}$$

In a wide band gap semiconductor such as ceria ($E_g \approx$ 6 eV), electron-hole pair formation due to thermal excitation is negligible. Therefore, the polaron concentration can be directly correlated to the bulk oxidation state, with $[Ce^{3+}]_{bulk} = c_{eon} / c_{eon}^0$, where $c_{eon}^0$ is the concentration of all Ce ions. This approach of correlating the thin film capacitance to the bulk oxidation state can be easily extended to non-dilute solutions by modifying the functional form of the chemical potential.

A typical impedance spectrum is shown in Figure S4 in the Nyquist form. A small high-frequency feature is visible, which is not predicted by the impedance model. It has been shown elsewhere that this feature is related to the electronic current constriction near the perimeter of the buried metal current collector.[4] We account for this effect by adding an additional resistor-capacitor network in series with equivalent circuit. Furthermore, we also observe that the main arc in the Nyquist plot takes a slightly depressed semi-circular shape, rather than a perfect half-circle. This non-ideal behavior can attributed to the dispersion in the characteristic frequency, for example, due to variation in the film thickness. To account for such non-ideality, we replace the ideal capacitor in the parallel resistor-capacitor network with a constant-phase element, with the impedance given as $Z_{CPE} = \left[ (j\omega)^m Y \right]^{-1}$, where $j = \sqrt{-1}$ and $\omega$ is the angular frequency. It can be shown that the equivalent capacitance of the constant-phase element is $C_{eq} = Y^{1/m} R^{1/m-1}$, where $R$ is the resistance. The modified equivalent circuit is fitted to the impedance spectrum, Figure S4. The surface capacitance ($C_{ion}^{ext}$) was reported elsewhere[1] to be approximately 4 mF cm$^{-2}$ and independent of temperature and pressure. Using Eq. (S2), the bulk $Ce^{3+}$ fraction is calculated from the fitted chemical capacitance.

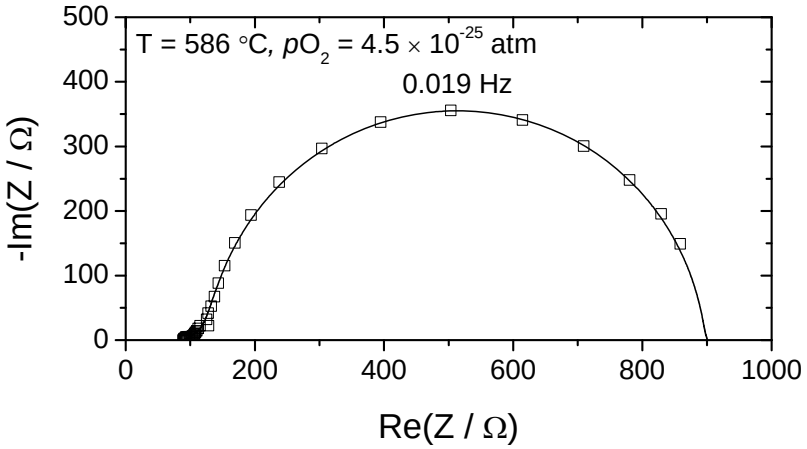


**Figure S4.** Typical measured (dots) and fitted (line) impedance spectrum in the Nyquist plot at zero-bias. Data collected *in-operando* during an APXPS experiment.

**XPS Quantification Procedure**

The $Ce^{3+}$ concentration was quantified using two independent methods based on (1) valence band (localized Ce 4*f*) and (2) core level (Ce 3*d*) photoelectron spectra. Upon removal of oxygen from ceria, the gap state located approximately 1.5 eV above the O 2*p* band edge appears and has been assigned to occupied, localized Ce 4*f* orbitals.[5-9] Accordingly, the peak area can be used to determine directly the average Ce oxidation state. Here, the Ce 4*f* integrated area is normalized to the Ce 4*d* area, the latter of which originates from both $Ce^{3+}$ and $Ce^{4+}$. The fraction of Ce in the 3+ oxidation state is given by:

$$[Ce^{3+}]_{surf} = \frac{A_{Ce\ 4f} \times \alpha_{Ce\ 4d}}{A_{Ce\ 4d} \times \alpha_{Ce\ 4f}} \qquad \textbf{(S3)}$$

where $\alpha_i = (\text{Photon Flux}) \bullet (\text{Cross Section}) \bullet (\text{Angular Efficiency})$ is the photon-energy-dependent normalization factor and $A$ is the integrated peak area (the entire peak area is used when no final state is indicated in the subscript). Photon flux was measured experimentally at the beamline using a calibrated photodiode whereas the theoretically-computed atomic subshell photoionization cross sections and asymmetry parameters were taken from reference 10. In this analysis, it is assumed that 4*f* occupancy is predominately in the gap state rather than in the O 2*p*-Ce 4*f* hybridized orbital, *i.e.*, it is

fully localized. It was verified experimentally that the gas-phase X-ray attenuation was not a strong function of $h\nu$ between 270 eV and 390 eV.

Turning to the core-level analysis, the $Ce^{3+}$ concentration was determined using a linear combination of two Ce 3*d* spectra:

$$[Ce^{3+}]_{surf} = 1 - \frac{A_{Ce\ 3d,u'''}}{A^{oxd}_{Ce\ 3d,u'''}} \frac{A^{oxd}_{Ce\ 3d}}{A_{Ce\ 3d}} \quad \textbf{(S4)}$$

where the superscript "oxd" indicates the reference spectra taken under a sufficiently oxidizing condition such that $[Ce^{3+}]_{surf}$ can be approximated as zero, and $u'''$ denotes the highest binding energy peak in the Ce 3*d* envelope. Here, a photoelectron spectrum collected at 465 °C and $7 \times 10^{-6}$ Torr $O_2$ is taken as the oxidized reference spectrum (Figure 3b). Under this condition, an occupied Ce 4*f* state in the band gap is completely absent and confirms the oxidized nature of ceria surface. This approach assumes that the mixed valent Ce 3*d* spectra is a linear combination of the fully oxidized and fully reduced spectra, and that the Ce $3d,u'''$ peak area scales linearly with $[Ce^{4+}]_{surf}$. These assumptions are generally valid for moderate values of $[Ce^{3+}]_{surf}$.[11]

Finally, the dopant (Sm) concentration was determined using:

$$[Sm]_{surf} = \frac{A_{Sm\ 3d} / \alpha_{Sm\ 3d}}{A_{Ce\ 4d} / \alpha_{Ce\ 4d} + A_{Sm\ 3d} / \alpha_{Sm\ 3d}} \quad \textbf{(S5)}$$

Because of the proximity of the Sm 4*d* and Ce 4*d* binding energies, the same photon energy was used ($h\nu$ = 390 eV) and the electron attenuation length was assumed to be the same. The quantification result is shown in Figure S5. A linear background was used for Ce 3*d*, Ce 4*d*, and Sm 4*d* photoemission, whereas a Shirley background was used for the valence band spectra.

To examine the consistency of the two quantification methods, $[Ce^{3+}]_{surf}$ determined from Ce 3*d* and Ce 4*f* analysis are plotted against each other in Figure S6. Overall, good linearity is obtained, with the slope close to 1.

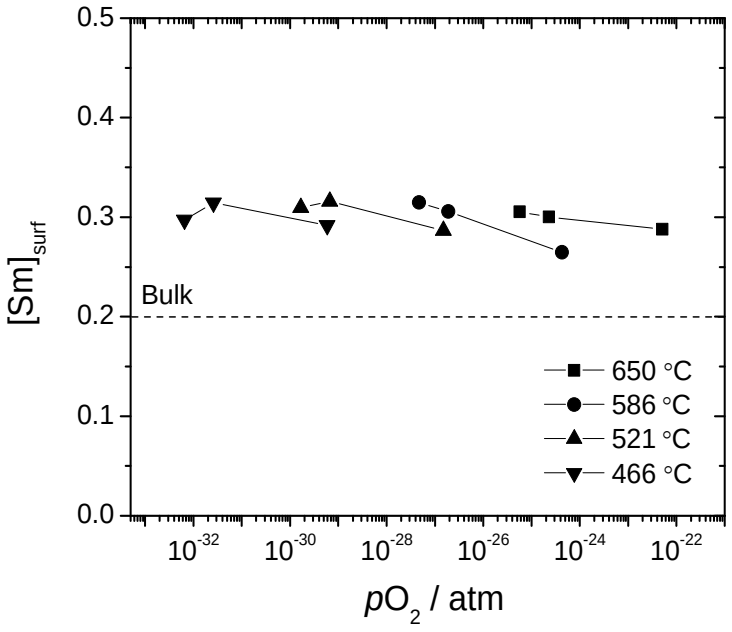


**Figure S5.** Surface Sm dopant fraction (relative to the total Sm and Ce concentration) as a function of temperature and oxygen activity. Dashed line indicates bulk dopant concentration quantified by electron probe microanalysis. Not plotted in is the Sm fraction at 465 °C and $7 \times 10^{-6}$ Torr $O_2$, $[Sm]_{surf} = 0.35$.

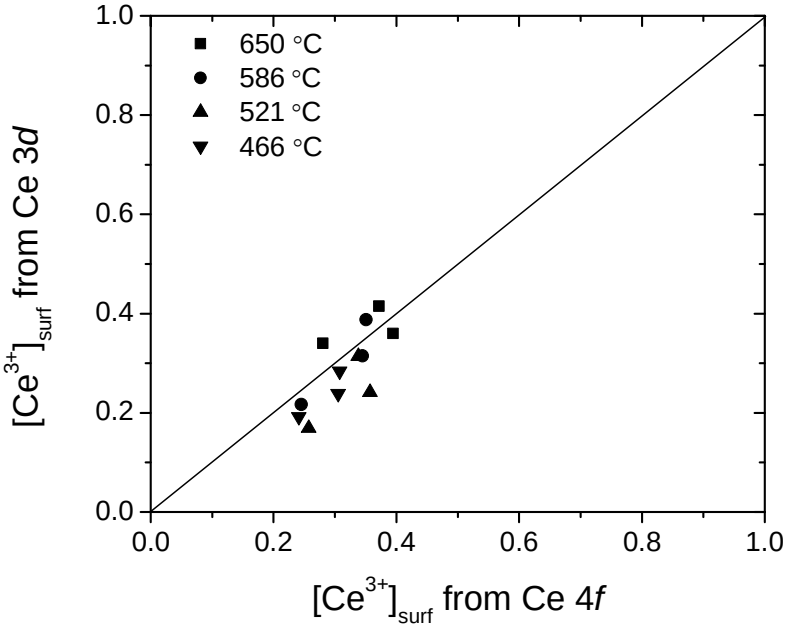


**Figure S6.** Self-consistency check for surface $Ce^{3+}$ fraction determined from Ce 4*f* and Ce 3*d* photoelectron peaks.

**Effective Attenuation Length**

*Calculation*

The effective attenuation length (EAL) was calculated using the NIST Standard Reference Database 82[12] based on the TPP-2M predictive equation for the electron inelastic mean free paths. The parameters used for the calculation are summarized in Table S1. Because the composition changes near the sample surface, it is important to examine how this affects the EALs. Specifically, the EALs were computed for two compositions: $Sm_{0.2}Ce_{0.8}O_{1.9}$ (bulk) and $Sm_{0.5}Ce_{0.5}O$. The variation in EALs was less than 6 % in the kinetic energy range examined. Therefore, the scattering properties are taken to be uniform within the sample.

| | |
|---|---|
| Composition | $Sm_{0.2}Ce_{0.8}O_{1.9}$ |
| Density | 7.2 g $cm^{-3}$ |
| Number of valence electron* | 20.4 |
| Asymmetry Parameter[10] | 0.770 ($h\nu$ = 270 eV) |
| Band gap** | 6 eV |
| X-ray incidence angle (with respect to surface normal) | 15 ° (Beamline 11.0.2)<br>75 ° (Beamline 9.3.2) |
| Electron emission angle (with respect to surface normal) | -40 ° (Beamline 11.0.2)<br>0 ° (Beamline 9.3.2) |

**Table S1.** Parameters used for calculating the effective attenuation length of Ce 4*f* photoelectrons. *The six 5*p* electrons in Ce are included in the valance electron count as they contribute strongly to the energy-loss spectrum.[13] ** Two values of band gap are reported in literature: the gap between valence band maximum and the localized Ce 4*f* (~ 3 eV) state, and the gap between the valence band maximum and the conduction band minimum (~ 6 eV). It is not immediately clear which value is more suitable in calculating the inelastic mean free path, though the calculated EALs differ by less than 3 %.

*Correction*

With the EALs calculated, it is possible to correct for the finite XPS penetration depth and estimate the composition on the topmost surface. The simplest approach is to approximate the sample as a bilayer structure, consisting of an overlayer (of thickness $t$) with an unknown composition and a substrate with a known composition. By integrating the mass attenuation equation (with intensity originating from depth $z$ given by $I = I_0 \exp\left(-z/(EAL\cos\alpha)\right)$, where $\alpha$ is the electron emission angle with respect to the surface normal), we obtain the following expression for the corrected composition of the surface overlayer:

$$[Ce^{3+}]_{ol} = \frac{[Ce^{3+}]_{surf} - [Ce^{3+}]_{bulk} \exp\left(-t/(EAL\cos\alpha)\right)}{1 - \exp\left(-t/(EAL\cos\alpha)\right)} \quad \textbf{(S6)}$$

To carry out this correction, the overlayer thickness needs to be specified. While this quantity is not available experimentally, a lower bound can be readily estimated. By recognizing that $[Ce^{3+}]_{ol}$ cannot exceed one and assuming that the layer thickness does not change with experimental conditions, one obtains:

$$1 \geq \frac{[Ce^{3+}]_{surf} - [Ce^{3+}]_{bulk} \exp\left(-t/(EAL\cos\alpha)\right)}{1 - \exp\left(-t/(EAL\cos\alpha)\right)} \quad \textbf{(S7)}$$

Because the EAL depends on the overlayer thickness, we solve the equation iteratively. Dopant concentration in the overlayer is estimated in the same manner.

Using Eq. (S7), the upper-bound limit for the $[Ce^{3+}]$ at the outermost surface is, for all temperature and pressure conditions, a factor of 2.5 - 2.6 greater than shown in Figure 2, with the lowest and highest values being 0.64 and 1.0, respectively. The variation of oxidation state with oxygen activity (*i.e.*, the slope in Figure 2) and the chemical potentials are essentially unchanged. Assuming the same segregation length scale for $Ce^{3+}$ and Sm, the upper-bound value for $[Sm]_{surf}$ in the outermost surface

ranges from 0.33 to 0.43, again, slightly exceeding the directly computed values. The lower bound thickness (~ 2 Å) of the outermost layer corresponds to approximately half the unit cell thickness in ceria ($a_o$ = 5.4 Å) and suggests that approximately two atomic planes in the (100) orientation are disrupted by the surface termination.

**Surface OH Concentrations**

Surface OH concentration was qualitatively assessed by comparing O 1*s* photoelectron spectra collected under humidified and dry conditions. We first measured the O1*s* spectra under $H_2$-$H_2O$ atmospheres at 650 °C. Subsequently, we evacuated the chamber to $<10^{-7}$ Torr at ~460 °C, backfilled with 7 x $10^{-6}$ Torr $O_2$, and collected an O 1*s* spectrum after equilibration. As evident in Figure S7, the spectra taken under dry and wet environments are qualitatively similar to each other and do not show a significant change in the high binding energy shoulder (OH is expected at ~2.5 eV above the lattice oxygen peak[14]). Based on temperature-programmed desorption results, OH on $CeO_2$ begins to decompose at ~230 °C.[14] Given our much higher sample temperature, we expect that any surface OH species would have desorbed from the surface at 460 °C under < $10^{-7}$ Torr. This data suggests that surface OH coverage is very low at 650 °C, particularly when compared to that of the $Ce^{3+}$ concentration. We did not attempt to analyze O1s spectra further due to the lack of reference spectra under high temperature, ambient pressure conditions. We speculate that the high binding energy shoulder could be due to surface lattice oxygen, surface oxygen vacancy defects, or impurities.

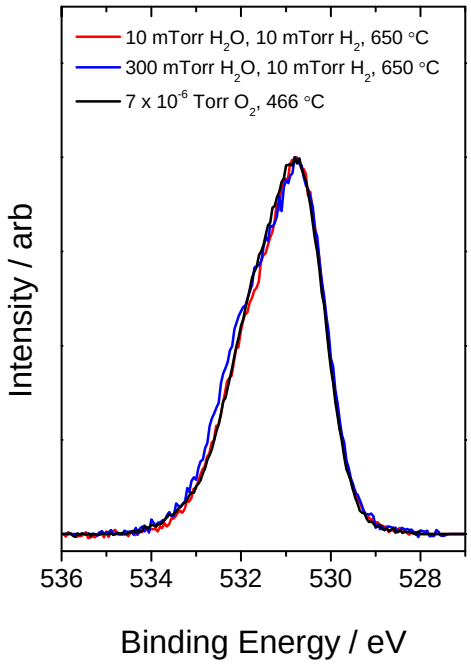


**Figure S7**: O 1*s* spectra at various conditions at 650 °C. For clarity, the binding energy of the lattice oxygen peak is aligned to that in the spectrum taken under oxidizing condition (slight energy shifts are observed due change in the electron chemical potential in ceria upon interaction with the gas). Intensity is also normalized to the lattice oxygen peak. Measured at a photon energy of 800 eV.

**REFERENCES**


(1) Chueh, W. C., California Institute of Technology, 2011.

(2) Jamnik, J.; Maier, J. *Phys. Chem. Chem. Phys.* **2001**, *3*, 1668.

(3) Kobayashi, T.; Wang, S.; Dokiya, M.; Tagawa, H.; Hashimoto, T. *Solid State Ionics* **1999**, *126*, 349.

(4) Brown, E., California Institute of Technology, 2011.

(5) Henderson, M. A.; Perkins, C. L.; Engelhard, M. H.; Thevuthasan, S.; Peden, C. H. F. *Surf. Sci.* **2003**, *526*, 1.

(6) Mullins, D. R.; Overbury, S. H.; Huntley, D. R. *Surf. Sci.* **1998**, *409*, 307.

(7) Ganduglia-Pirovano, M. V.; Hofmann, A.; Sauer, J. *Surf. Sci. Rep.* **2007**, *62*, 219.

(8) Pfau, A.; D., S. K. *Surf. Sci.* **1994**, *321*, 71.

(9) Mullins, D. R.; Radulovic, P. V.; Overbury, S. H. *Surf. Sci.* **1999**, *429*, 186.

(10) Yeh, J. J.; Lindau, I. *Atomic Data and Nuclear Data Tables* **1895**, *32*, 1.

(11) Shyu, J. Z.; Otto, K.; Watkins, W. L. H.; Graham, G. W.; Belitz, R. K.; Gandhi, H. S. *J. Catal.* **1988**, *114*, 23.

(12) Powell, C. J.; Jablonski, A. *NIST Electron Effective-Attenuation-Length Database Version 1.3, SRD 82*; National Institute of Standards and Technology: Gaithersburg, MD, 2011.

(13) Tanuma, S.; Powell, C. J.; Penn, D. R. *Surf. Interface Anal.* **2003**, *35*, 268.

(14) Kundakovic, L.; Mullins, D. R.; Overbury, S. H. *Surf. Sci.* **2000**, *457*, 51.